The 9th European Congress on Computational Methods in Applied Sciences and Engineering
ECCOMAS Congress 2024
3–7 June 2024, Lisboa, Portugal

SIMULATING TWO-PHASE FLOW WITH A SHARP, STRUCTURE-PRESERVING TWO-VELOCITY MODEL

ARTHUR E. P. VELDMAN[1*] AND RONALD A. REMMERSWAAL[1,2]

[1] Bernoulli Institute, University of Groningen
Nijenborgh 9, 9747AG Groningen, The Netherlands
e-mail: a.e.p.veldman@rug.nl, www.rug.nl

[2] Max Planck Institute for Plasma Physics
D-85748 Garching, Germany
e-mail: ronald.remmerswaal@ipp.mpg.de

Key words: Multiphase Flow, Sharp Interface, Two-velocity Model, Structure-Preserving Discretization, Finite Volume

Summary. The paper presents a numerical simulation method for two-phase flow at high Reynolds numbers, intended to describe the development of flow instabilities (Kelvin–Helmholtz, Rayleigh–Taylor) at the liquid-gas interface. Numerical diffusion has to be restricted to a bare minimum. To reach this goal, several enhancements have been made with respect to the existing CFD methods for two-phase flow: a parabolic reconstruction of the interface to suppress spurious velocities; a structure-preserving discretization to ensure a correct discrete exchange between potential and kinetic energy; and a two-velocity model featuring a discontinuous tangential velocity to approximate the unresolved viscous shear layer along the interface. Examples are presented for tips of breaking waves.

1 INTRODUCTION

The presented research originates in an engineering project concerning the transport of liquefied natural gas (LNG) or liquefied hydrogen (LH2) in carrier ships. Especially the impact of the liquid sloshing against the walls of cargo tanks is of major concern as it determines the structural strength of the tank construction. With the recent geopolitical developments, this application has even further increased in relevance. In the Sloshel project, research by the Maritime Research Institute MARIN (Wageningen) and GTT (Paris), one of the largest designers of LNG cargo tanks, has revealed that the peak impact force is largely determined by the instabilities (Kelvin–Helmholtz, Rayleigh–Taylor) that form when the breaking wave tip approaches the tank walls (Figure 1) [8]. Yet, existing CFD simulation methods are not able to accurately predict these instabilities. Thus, a large project on sloshing in LNG tanks (SLING) was intiated by MARIN, sponsored by the Dutch science foundation NWO and the offshore industry.

The scientific CFD developments in the project concerning the generation of surface instabilities are described in this paper. Its main numerical challenge is to design a numerical method that stays numerically stable, yet at the same time allows physical instabilities to form. This implies that numerical dissipation has to be restricted to a bare minimum, whereas the discretization should take care of a correct exchange between the three forms of energy: potential, kinetic and surface energy.

2 NUMERICAL METHOD

2.1 Overview

The most crucial part of a simulation method for two-phase flow at high Reynolds numbers is the way in which the fluids (e.g. LNG and its vapor) are coupled at the liquid-gas interface. Viscous effects play a role at this interface, but result in a shear layer which is very thin and expensive to resolve. We propose to model this shear layer with a tangential velocity discontinuity, resulting in a novel and truly sharp two-velocity model. In this model, each fluid gets its own velocity and corresponding momentum conservation law; see Section 2.3.

The resulting incompressible, two-phase Navier–Stokes equations are solved using a finite-volume method on an adaptive 3D mesh with a staggered positioning of the unknowns, as implemented in the in-house free-surface method ComFLOW [1]. Capillary effects due to surface tension are included in the model, and actually play a significant role in the flow physics. In Section 2.2 we will describe which improvements we have made in the reconstruction of the interface.

A dimensionally unsplit geometric volume of fluid (VOF) method advects the interface. Mass transport is performed by an extension of the Lagrangian EMFPA method of Hernandez et al. [7] which was improved by Owkes and Desjardins [11]; see Figure 2. This results in a sharp representation of the interface, without any occurrence of 'overful' and 'underempty' cells. The transport of momentum is done using the same volume fluxes as used for mass transport [16]. An algebraic interpolation of the fluxes is proposed, resulting in exact mass and momentum conservation, while obtaining semi-discrete conservation of kinetic energy, and an almost perfect exchange with potential and (capillary) surface energy. Section 2.4 gives some more details.

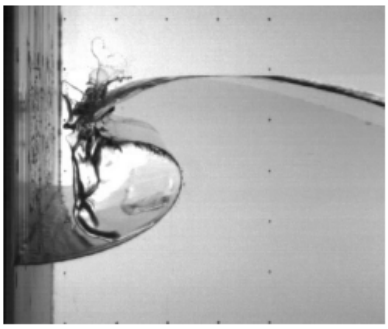

Figure 1: Instabilities appear at a breaking-wave tip shortly before impact.

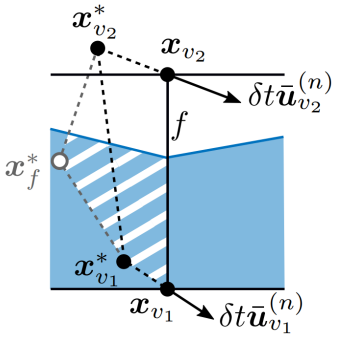

Figure 2: The modified EMFPA advection method.

2.2 Reconstruction and curvature

The effects of surface tension are proportional to the curvature of the liquid-gas interface, as a consequence of the Young–Laplace law. Therefore, simulating capillary flow sets high requirements to the accuracy with which the reconstruction and advection of the interface is carried out. To quantify this issue, we have performed a simulation of a circular droplet that is being stretched and then returned to its original shape; see Figure 3 (left). The curvature at the end of this stretching process is used to monitor the numerical errors.

In our first simulations we have reconstructed the interface using a PLIC method [18], which approximates the interface with piecewise linear polynomials. It has been combined with two methods to compute the normals to the interface: the ELVIRA method of Pilliod and Pucket [12], and the MOF method of Dyadechko and Shashkov [3]. Grid refinement has been studied to see whether the error in the curvature goes to zero. In Figure 3 (right) the behavior of the curvature error is shown: the error does not diminish when the grid is refined. This also happens when a local height function (LHF) [5] is used to reconstruct the interface (not shown in the graph). It is found that this inaccuracy is an important source for the spurious velocities that are usually seen. Also, note that these unphysical velocities contain energy, which disturb the energy budgets that contribute to the formation of physical instabilities.

In his PhD thesis [14], Remmerswaal has theoretically shown that this behavior is to be expected. He also showed that to achieve grid convergence it is necessary to reconstruct the free surface with at least second-order accuracy, i.e. using a piecewise parabolic approximation (PPIC); see also [15]. Our numerical simulations using such a parabolic approximation combined with ELVIRA, MOF and the LHF, confirm this analysis, as visible in Figure 3 (right). The spurious energy leakage and the corresponding amount of unphysical velocities also has significantly decreased.

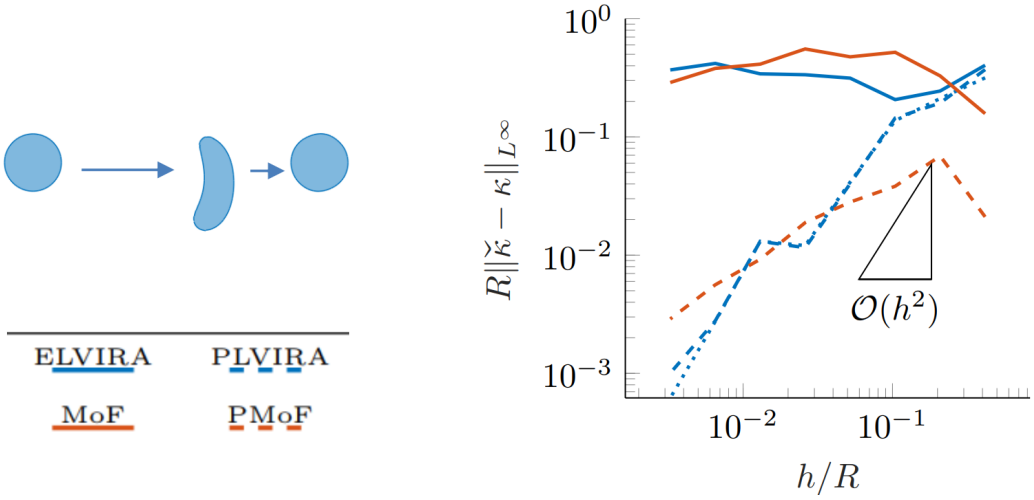

Figure 3: Grid-refinement error in the curvature after stretching a droplet, using piecewise linear (PLIC, solid lines) and piecewise parabolic (PPIC, dashed lines) reconstructions.

2.3 Two-velocity model

When the Reynolds number is large, the shear layer thickness is much less than the capillary length scale. As the capillary scales are already expensive to resolve, also resolving viscous shear layers becomes computationally prohibitive. Therefore, it was decided to model the interface shear layer as a discontinuity in the tangential velocity component. Note that this is similar to solving the Euler equations with a slip condition along solid walls.

As a result, we end up with two phases (gas and liquid) with two velocities u^π and two pressures p^π, where $\pi \in \{g, l\}$ representing gas and liquid, respectively. Jumps across the

interface will be denoted as $[[u]] \equiv u^g - u^l$ and similar for p. These jumps are treated with a conservative multi-dimensional version of the ghost fluid method (CMDGFM) [14], which is an extension of the GFM method of Liu et al. [10].

Technical details

The jump in tangential velocity leads to a jump in the normal pressure gradient, as explained next. Hereto, let us start with the semi-discrete momentum equation, which for incompressible flow can be turned into a Poisson equation:

$$\mathbf{u}^{\pi,(n+1)} = \mathbf{u}^{\pi,*} - \frac{\delta t}{\rho^\pi}\nabla p^\pi \quad \Rightarrow \quad \nabla\cdot\left(\frac{1}{\rho^\pi}\nabla p^\pi\right) = \frac{1}{\delta t}\nabla\cdot\mathbf{u}^{\pi,*}.$$

Here, $\mathbf{u}^{\pi,*}$ collects $\mathbf{u}^{\pi,(n)}$ and all convective, diffusive and body-force terms from the momentum equation.

The normal velocity $u_\eta^{(n+1)} \equiv \mathbf{u}^{\pi,(n+1)}\cdot\boldsymbol{\eta}$ is assumed to be continuous, which leads to a jump in the normal derivative of the pressure

$$\left[\!\left[\frac{1}{\rho}\frac{\partial p}{\partial \eta}\right]\!\right] = \frac{[[u_\eta^*]]}{\delta t}.$$

Furthermore, the pressure has a capillary jump across the interface due to the effect of surface tension, given by the Young–Laplace equation

$$[[p]] = -\sigma\kappa,$$

where κ is the curvature of the interface.

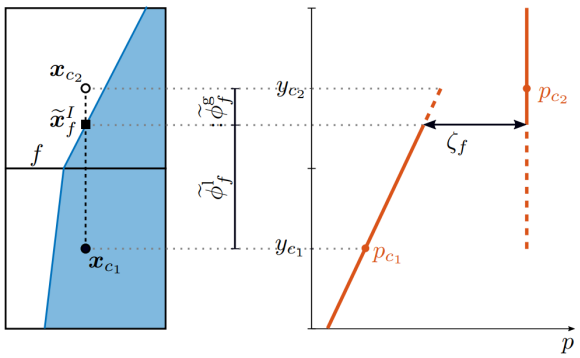

Figure 4: Sketch of the GFM approach for the pressure near the interface.

Figure 5 gives an illustration of the performance of the two-velocity model. The left-hand graph shows the velocity amplitude near the tip of a breaking wave computed on a very fine grid and using the traditional one-velocity model; the top figure is a close-up near the wave tip. In the middle graph the one-velocity model is applied on a coarse grid, in which the mesh size is 32× larger. The lower graph shows much activity in the gas region, which is an entrainment effect of the velocity of the liquid; in popular wordings, the liquid generates a 'storm' in the air. Such pictures are very common in one-velocity simulations. In contrast, the righ-hand graph shows the two-velocity solution on the same coarse grid (the grid can be recognized on the top graph). By comparing with the left-hand graph, it is seen that the velocity field near the wave tip is visually equal to the velocity field on the very fine grid, These simulations were done with adaptive grid refinement, but if they were done on a uniform grid, the coarse-grid simulation with the two-velocity model would be $32^4 \approx 10^6\times$ cheaper (note that also the time step can be taken 32× larger).

Relation with one-velocity model

The relation with the one-velocity model is further illustrated by detailed simulations of the breaking wave a shown in Figure 6(a). In Figure 6(b) we see the tangential velocity of the one-

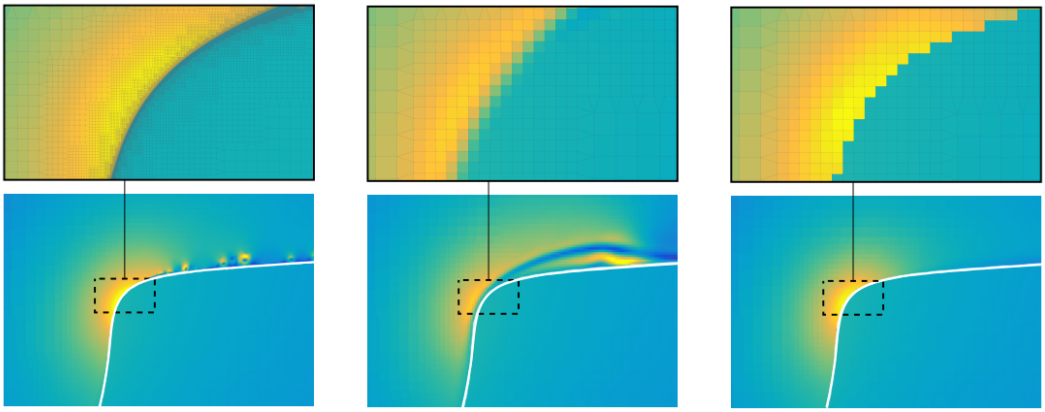

A. Fine mesh using the one-velocity formulation.

B. Coarse mesh using the one-velocity formulation.

C. Coarse mesh using our proposed two-velocity formulation.

Figure 5: Comparison of the two-velocity model with the one-velocity model. The left-hand graph shows the velocity around a breaking wave tip on a very fine grid. The other two graphs show results on a 32× coarser grids: in the middle graph a one-velocity model is used, whereas the right-hand graph shows the results of the new two-velocity model.

and two-velocity solutions, corresponding with the inset in Figure 6(a). The colored markers depict the jump in tangential velocity for the various grid resolutions: blue symbols correspond with the coarsest grid, red is 2× finer and green 4×, whereas black symbols correspond with an 8× finer grid. The dashed lines show the one-velocity solution, with the same color code. It is clearly visible that on the coarser grids the shear layer is much too thick. But it also shows that upon grid refinement the two sets of solutions converge to each other.

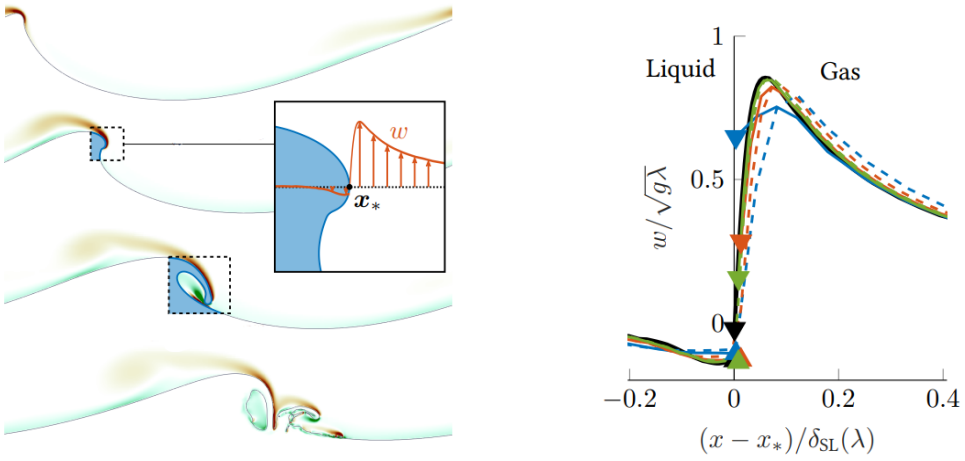

(a) Breaking wave overview.

(b) Velocity jump.

Figure 6: Grid refinement of the one- and two-velocity solution around the interface.

2.4 Discrete energy preservation

Convective preservation of kinetic energy Let the analytic and semi-discrete equations for conservation of mass and momentum by given by

$$\begin{aligned} \textit{mass:} \qquad & \frac{\partial \rho}{\partial t} + \nabla\cdot\mathbf{m} = 0 \;\rightarrow\; \Omega\frac{\mathrm{d}}{\mathrm{d}t}\rho + \mathcal{D}_{\mathrm{mass}}\mathbf{m} = 0, \\ \textit{momentum:} \qquad & \frac{\partial \rho\phi}{\partial t} + \nabla\cdot(\mathbf{m}\phi) = ... \;\rightarrow\; \Omega\frac{\mathrm{d}}{\mathrm{d}t}(\rho\phi) + \mathcal{C}^{\mathbf{m}}_{\mathrm{mom}}\phi = ..., \end{aligned}$$

where Ω contains the volumes of the control volumes. Then it has been proven in [2, 16, 17] that a close relation has to exist between discrete mass transport and discrete momentum transport. In particular, assuming a volume-consistent scaling [16] as in the above discretization, kinetic energy is convectively preserved if and only if

$$\mathcal{C}^{\mathbf{m}}_{\mathrm{mom}} - \tfrac{1}{2}\mathrm{diag}(\mathcal{D}_{\mathrm{mass}}\mathbf{m}) \textit{ is skew-symmetric.}$$

This property has to hold for each of the phases individually, which is indeed the case for our convective discretization as detailed in the PhD thesis [14].

Exchange between gravitational potential energy and kinetic energy Also, a correct exchange between kinetic energy and potential energy has been pursued. This requires the definition of a gravitational potential energy function, which influences the discretization of the gravitational force in the momentum equation. This function is built using the first moment of the liquid position in a cell. In turn, by demanding well-posedness of the gravitational term, it also influences the discretization of the pressure gradient. Details of this mimetic gravity model (MGM) can be found in Section 7.6 of the before-mentioned thesis [14].

Exchange between capillary surface energy and kinetic energy To safeguard a correct exchange of kinetic and surface energy, a mimetic surface tension model (MSTM) is under development; we hope to report on it at future occasions. An important ingredient is a geometric relation between the interface area and the face and volume apertures that describe the position of the liquid, in order to link the two types of energy (per surface area versus per volume); see Section 4.6 of [14].

3 SIMULATIONS

3.1 Verification: Kelvin-Helmholtz with surface tension

In our first demonstration we verify whether the surface tension effects are correctly described by our numerical model. We do so by comparing the numerical results with analytical predictions of the evolution of (capillary) Kelvin–Helmholtz waves. For interface waves with wave length λ, wave number k and temporal evolution $e^{-\mathrm{i}\aleph_\pm t}$, their dispersion relation is given by

$$\aleph_\pm = k\frac{\rho u_\tau}{\rho} \pm \frac{2\pi}{T_\sigma}\sqrt{1-\mathrm{We}} \;\text{ with Weber number } \mathrm{We} = \frac{\rho^g\rho^l[[u_\tau]]^2\lambda}{2\pi\sigma(\rho^g+\rho^l)},$$

where $T_\sigma = \sqrt{(\rho^l+\rho^g)\lambda^3/2\pi\sigma}$ is the capillary time scale. It can be seen that for large values of the surface tension σ, i.e. low Weber numbers ($\mathrm{We} \leq 1$), the temporal frequency $\aleph_\pm$ is real,

whereas for large Weber numbers (We $>$ 1) it is imaginary (leading to exponentially growing waves). Thus, surface tension stabilizes a Kelvin–Helmholtz instabilty when the Weber number is sufficiently low. We have checked the dispersion relation by carrying out simulations for a range

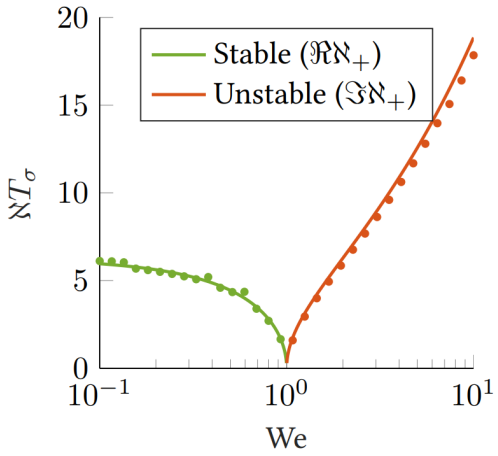

Figure 7: The real and imaginary part of the temporal frequency $\aleph_\pm$ for low and high Weber numbers, respectively: analytical versus numerical.

of Weber numbers. Figure 7 gives the comparison between the numerically found dispersion relation and the analytical one [9, Art. 267 & 268]. In the stable range, for We $<$ 1, the real part of $\aleph T_\sigma$ is plotted, whereas for We $>$ 1 the imaginary part is plotted. Excellent agreement is obtained, showing that the flow near the interface is very well described by our model, regardless of the Weber number.

3.2 Breaking wave tip at various scales

In the following example we show the influence of surface tension on the onset of instabilities. The test case concerns a breaking wave, computed at various scales s ranging from 40 down to 5. With increasing s the geometric length scale $\lambda^{1:s}$ decreases. As a consequence, the influence of surface tension is largest at the larger values of s. This also shows in Figure 8 which depicts the evolution of the wave tip at various values of s. At the largest scale 1 : 40 the interface stays nicely smooth, at smaller scales instabilities develop, culminating in the smallest scale 1 : 5.

3.3 Comparison with other codes

Next we show detailed results from our two-velocity model of the flow near a breaking wave tip in the simulation of a large gas pocket impact (LGPI) [4] at a scale 1:40. The typical length scale is $\lambda^{1:40} = \lambda/40 = 0.5$ m. The computational grid starts with a uniform basis grid with $h_0 = \lambda^{1:40}/80$. Near the wave tip it has been refined with 7 levels, which results in a smallest mesh width given by $h \approx 10^{-4}\,\lambda^{1:40} \approx 5 \times 10^{-5}$ m.

Our results have been compared with those of two other CFD methods: the CADYF code developed at the University of Montreal [6], and the Basilisk code developed in Paris [13]. CADYF is an arbitrary Lagrangian Eulerian (ALE) finite-element method. The mesh is adapted according to an error estimate, resulting in a minimal mesh size of $h \approx 2 \times 10^{-4}\lambda^{1:40} \approx 10^{-4}$ m.

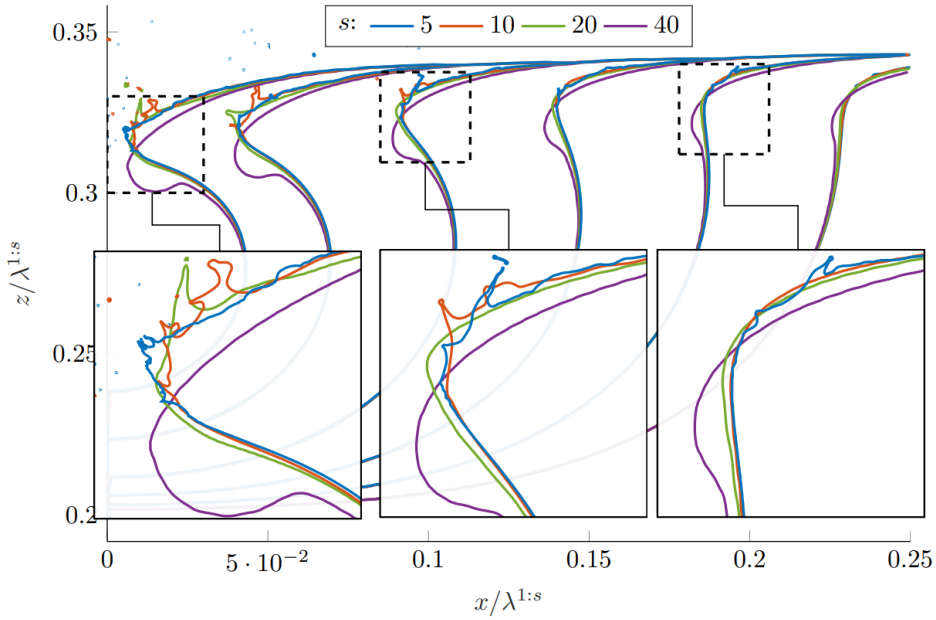

Figure 8: Evolution of the tip of a breaking wave at various scales: the larger the scale, the more influence from surface tension.

Basilisk is an open source finite-volume method based on an adaptive quad/oct-tree mesh. For Basilisk we consider an underlying coarse grid with mesh width $h_0 = 2^{-7}\lambda^{1:40}$, and we used up to 6 levels of additional mesh refinement, resulting in $h = 2^{-13}\lambda^{1:40} \approx 6 \times 10^{-5}$ m.

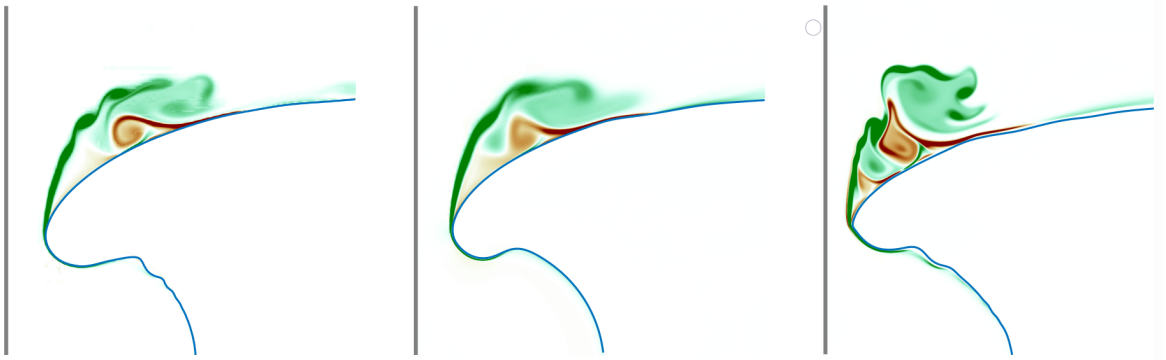

A. ComFLOW. **B.** CADYF. **C.** Basilisk.

Figure 9: Comparison between three different CFD methods of the vorticity near the tip of a breaking wave in a large gas-pocket impact (LGPI).

Thus, near the wave tip, the three codes have a comparable grid size, allowing for a fair comparison. Figure 9 shows the y-component of the vorticity for the three simulations. Especially the agreement between ComFLOW and CADYF is excellent. The latter is slightly more diffusive, which is due to the (small amount of) numerical diffusion which is common in finite-element simulations. Above the wave tip the Basilisk results are different from these two

simulations, but below the tip Basilisk shows similar oscillations as ComFLOW (which are not visible in the CADYF results).

3.4 Rayleigh–Taylor instability

Our final example concerns three-dimensional flow. When a wave tip is progressing forward it is accelerating, with the heavier fluid (liquid) behind the lighter fluid (air). This situation is comparable when we consider the gravitational acceleration with the heavier fluid above the lighter one. That means that also along such an accelerating wave tip a Rayleigh–Taylor instability can develop, and the analytical formula for the most unstable wave length does apply [9, Art. 267]:

$$\lambda_{RT} = \frac{2\pi}{k_{RT}} = \sqrt{\frac{12\pi^2\sigma}{(\rho^l - \rho^g)\mathbf{g}\cdot\boldsymbol{\eta}}}$$

Figure 10 shows a snapshot of the simulation. The wave length of the observed instabilities is found consistent with the above analytical formula.

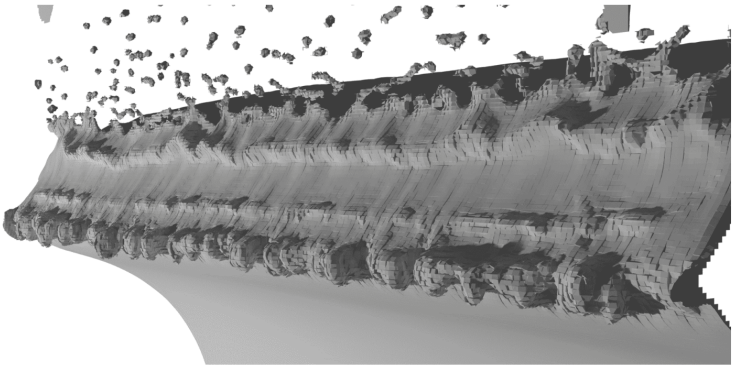

Figure 10: Development of a Rayleigh–Taylor instability along the tip of an accelerating breaking wave.

4 CONCLUDING REMARKS

In the manuscript we have discussed the numerical simulation of two-phase flow, in high-Reynolds number applications featuring the development of instabilities. This creates a balancing act between numerical stability and numerical diffusion. To reduce the amount of numerical diffusion most of the numerical ingredients in the CFD method had to be refined. In particular, we have introduced:

- a parabolic reconstruction of the liquid-gas interface;

- a structure-preserving discretization with exact exchange between all three forms of energy;

- a two-velocity model to circumvent the resolution issues of the interface shear layer.

Whereas the traditional one-velocity model results in an artificial thickening of the shear layer, the two-velocity model instead sharply and accurately approximates the unresolved shear layer with a velocity discontinuity. We do not neglect viscous stresses altogether, and in fact mesh

refinement of the two-velocity model yields the same solution as obtained with the one-velocity model. Our approach greatly reduces the required number of grid points (i.e. computational cost), making simulations of breaking wave impacts better affordable.

The proposed numerical method has been validated using several academic flow problems of surface instabilities (Kelvin–Helmholtz, Rayleigh–Taylor), and was applied to several wave impact problems (e.g. sloshing in liquid storage tanks). Validation experiments featuring impacting breaking waves are underway at MARIN.

Acknowledgements

This work is part of the research programme SLING, which is (partly) financed by the Netherlands Organisation for Scientific Research (NWO).

REFERENCES

[1] ComFLOW. Website: `www.math.rug.nl/∼veldman/comflow/comflow.html`. User Group: `www.marin.nl/en/jips/networks/comflow-user-group`.

[2] G. Coppola and A. E. P. Veldman. Global and local conservation of mass, momentum and kinetic energy in the simulation of compressible flow. *Journal of Computational Physics*, 475:111879, 2023.

[3] V. Dyadechko and M. Shashkov. Moment-of-fluid interface reconstruction. *Los Alamos Report LA-UR-05-7571*, 49, 2005.

[4] S. Etienne, Y.-M. Scolan, and L. Brosset. Numerical study of density ratio influence on global wave shapes before impact. In *International Conference on Offshore Mechanics and Arctic Engineering*, volume 51302, page V009T13A025. American Society of Mechanical Engineers, 2018.

[5] J. Gerrits and A. E. P. Veldman. Dynamics of liquid-filled spacecraft. *Journal of Engineering Mathematics*, 45(1):21–38, 2003.

[6] A. Hay, S. Etienne, and D. Pelletier. Adaptive simulation of gas-liquid interfacial flows with surface tension. In *54th AIAA Aerospace Sciences Meeting*, page 1594, 2016.

[7] J. Hernandez, J. Lopez, P. Gomez, C. Zanzi, and F. Faura. A new volume of fluid method in three dimensions - Part I: Multidimensional advection method with face-matched flux polyhedra. *International Journal for Numerical Methods in Fluids*, 58:897–921, 2008.

[8] W. Lafeber, H. Bogaert, and L. Brosset. Elementary Loading Processes (ELP) involved in breaking wave impacts: findings from the Sloshel project. In *Proceedings 22nd International Offshore and Polar Engineering Conference*, Rhodes (Greece), June 17-23, 2012.

[9] H. Lamb. *Hydrodynamics (sixth edition)*. Cambridge University Press, 1932.

[10] X.-D. Liu, R. P. Fedkiw, and M. Kang. A boundary condition capturing method for Poisson's equation on irregular domains. *Journal of Computational Physics*, 160:151–178, 2000.

[11] M. Owkes and O. Desjardins. A mass and momentum conserving unsplit semi-lagrangian framework for simulating multiphase flows. *Journal of Computational Physics*, 332:21–46, 2017.

[12] J. E. Pilliod Jr and E. G. Puckett. Second-order accurate volume-of-fluid algorithms for tracking material interfaces. *Journal of Computational Physics*, 199(2):465–502, 2004.

[13] S. Popinet and collaborators. Basilisk, 2013. `http://basilisk.fr`.

[14] R. A. Remmerswaal. *Numerical Modelling of Variability in Liquid Impacts*. PhD thesis, University of Groningen, 24 January 2023.

[15] R. A. Remmerswaal and A. E. P. Veldman. Parabolic interface reconstruction for 2d volume of fluid methods. *Journal of Computational Physics*, 469:111473, 2022.

[16] A. E. P. Veldman. A general condition for kinetic-energy preserving discretization of flow transport equations. *Journal of Computational Physics*, 398:108894, 2019. doi:10.1016/j.jcp.2019.108894.

[17] A. E. P. Veldman. Supraconservative finite-volume methods for the Euler equations of subsonic compressible flow. *SIAM Review*, 63:756–779, 2021.

[18] D. L. Youngs. Time-dependent multimaterial flow with large fluid distortion. In K. W. Morton and M. J. Baines, editors, *Numerical Methods for Fluid Dynamics*, pages 273–285. Academic Press, New York, 1982.